NASA Technical Memorandum 106421

Army Research Laboratory
Technical Report ARL–TR–331

Experimental and Computational Results From a Large Low-Speed Centrifugal Impeller

M.D. Hathaway
Vehicle Propulsion Directorate
U.S. Army Research Laboratory
Lewis Research Center
Cleveland, Ohio

and

R.M. Chriss, J.R. Wood, and A.J. Strazisar
Lewis Research Center
Cleveland, Ohio

Prepared for the
82nd Meeting of the AGARD Propulsion and Energetics Panel, Technology Requirements for Small Gas Turbine Engines
sponsored by the Advisory Group for Aerospace Research and Development
Montreal, Canada, October 4–8, 1993

NASA

U.S. ARMY ARL RESEARCH LABORATORY

EXPERIMENTAL AND COMPUTATIONAL RESULTS FROM A LARGE LOW-SPEED CENTRIFUGAL IMPELLER

M. D. Hathaway
U. S. Army Vehicle Propulsion Directorate
21000 Brookpark Road
Cleveland, Ohio 44135, USA

R. M. Chriss, J. R. Wood, and A. J. Strazisar
NASA Lewis Research Center
21000 Brookpark Road
Cleveland, Ohio 44135, USA

SUMMARY

An experimental and computational investigation of the NASA Low-Speed Centrifugal Compressor (LSCC) flow field has been conducted using laser anemometry and Dawes' 3D viscous code. The experimental configuration consists of a backswept impeller followed by a vaneless diffuser. Measurements of the three—dimensional velocity field were acquired at several measurement planes through the compressor. The measurements describe both the throughflow and secondary velocity field along each measurement plane and in several cases provide details of the flow within the blade boundary layers. The experimental and computational results provide a clear understanding of the development of the throughflow momentum wake which is characteristic of centrifugal compressors.

NOMENCLATURE

J	Streamwise measurement grid indice
m/m_s	Non-dimensional shroud meridional distance
PS	Pressure surface
r/r_t	Radius non-dimensionalized by exit tip radius
SS	Suction surface
U_t	Impeller tip speed, m/sec
V_{qm}	Quasi-meridional velocity component, m/sec
V_r	Radial velocity component, m/sec
V_s	Spanwise secondary velocity component, positive towards the shroud, m/sec
V_z	Axial velocity component, m/sec
α	Flow pitch angle, deg., $\alpha = tan^{-1}(V_r/V_z)$

INTRODUCTION

The complex curvature of centrifugal compressor impeller blade channels, coupled with strong rotational forces and clearance between the rotating impeller and stationary shroud, generate secondary flows in unshrouded impellers which transport low momentum fluid into the main stream of the impeller passage. The ability to reduce the resultant flow nonuniformities at the impeller exit by altering new impeller designs to control the secondary flow development may therefore lead to improved performance. In order to succeed, such a design activity must be guided by an improved understanding of the flow physics within the impeller and by reliable numerical flow field predictions.

Several previous investigators have provided flow field measurements within unshrouded centrifugal compressor impellers. Eckardt's laser anemometer measurements in a radial-outflow impeller provided the first experimental evidence in high-speed impellers of the development of a "wake" of low momentum fluid near the suction surface/shroud corner of the blade passage, Eckardt[5]. Krain[12], Krain and Hoffman[14], Ahmed and Elder[1], Sipos[18], and Rohne and Banzhaf[16] have acquired laser anemometer measurements in backswept impellers which indicate that the wake develops near the shroud at mid-pitch.

Due to the small passage size and optical access limitations in these previous investigations, few experimental details of the secondary flow development inside high—speed impeller passages are available. Krain[12] and Sipos[18] have therefore used vortex models to infer the vortical nature of the secondary flow from the flow angle measurements which they were able to acquire on blade-to-blade streamsurfaces.

Several low-speed investigations have also provided some insight into secondary flows. Senoo, *et al.*,[17] used dye in a water-flow experiment to visualize the tip clearance flow. Farge, *et al.*,[7] performed 5–hole pressure measurements in a 1 meter diameter shrouded impeller which rotated at 500 rpm. A clearance gap was left between the blade tip and the impeller shroud in order to generate a tip clearance flow. However, as the authors point out, there is no relative motion between the blade and the shroud, so the physics of the tip clearance flow in this investigation is not the same as it would be in an unshrouded impeller. Fagan and Fleeter[6] used laser anemometry to measure all three velocity components in a low speed, shrouded, mixed-flow compressor.

In lieu of detailed experimental measurements of the secondary flow fields in unshrouded impellers, several investigators have recently shown secondary flow details generated using three—dimensional Navier-Stokes numerical simulations (Krain and Hoffman[13,14]; Hah and Krain[8]; Bansod and Rhie[3]; Moore and Moore[15]). Fagan and Fleeter[6] have also shown calculated secondary flow field results for their shrouded impeller.

The purpose of the present investigation is to provide a detailed experimental study of primary and secondary flow development within an unshrouded centrifugal compressor impeller. Laser anemometer measurements and surface flow visualization results are presented and compared to a prediction of the flow field generated using Dawes' three-dimensional

Navier-Stokes code, Dawes[4]. The processes which lead to the formation of the throughflow momentum wake which is characteristic of unshrouded centrifugal compressor impellers are clearly explained using results from both the CFD and experimental effort.

TEST COMPRESSOR AND INSTRUMENTATION

The NASA Low-Speed Centrifugal Compressor (LSCC) is an experimental facility designed to duplicate the essential flow physics of high-speed subsonic centrifugal compressor flow fields in a large low-speed machine in which very detailed investigations of the flow field can be made. A complete description of the facility is provided by Wood, *et al.*[19] and Hathaway, *et al.*[9].

The test compressor is a backswept impeller with a design tip speed of 153 m/sec. The impeller is followed by a vaneless diffuser in order to generate an axisymmetric outflow boundary condition which is desirable for CFD analysis of an isolated blade row. The impeller has 20 full blades with a backsweep of 55 degrees. The inlet diameter is 0.870 m and the inlet blade height is 0.218 m. The exit diameter is 1.524 m and the exit blade height is 0.141 m. The tip clearance between the impeller blade and the shroud is 2.54 mm, and is constant from the impeller inlet to the impeller exit. This tip clearance is 1.8% of the blade height at the exit of the impeller. The blade surfaces are composed of straight-line elements from hub to tip. This feature enabled fabrication of the impeller by a flank-milling process on a 5-axis milling machine. This feature also facilitates acquisition of laser anemometer measurement of velocities close to the blade surfaces by enabling the laser anemometer optical axis to be directed parallel to the blade surface.

The research operating point selected for both computational and experimental investigations of the LSCC flow field was set at standard–day corrected conditions of 30 kg/sec and 1862 rpm, which is near the design point, for all data presented herein.

A two-component laser fringe anemometer operating in on-axis backscatter mode was used in this investigation. Frequency shifting was used for both fringe systems to provide directional sensitivity for all velocity measurements. In order to determine all three components of the total velocity vector at a point in the flow field, two velocity components are measured at each of two different orientations of the laser anemometer optical axis. The resultant four measured components are combined using a least squares fit to yield the total three-dimensional velocity vector. A digital shaft angle encoder triggered by a once-per-rev signal generates 200 measurement intervals per blade pitch which are used to tag each velocity measurement with the circumferential measurement interval at which it occurred. Polystyrene latex spheres (0.80 to 0.95 μm dia.) injected in the plenum were used as seed material.

A meridional view of the LSCC, see Figure 1, shows the spanwise and streamwise locations at which laser anemometer data have been acquired. The cross-channel measurement stations which are numbered denote the stations at which data will be presented. The station numbers are the streamwise indices of a body-fitted measurement grid which was used to position the laser measurement point within the impeller. The measurement grid used in this investigation divides the streamwise blade length into a series of "quasi-orthogonal", or near-normal, cross-channel planes. Further details on the instrumentation are provided by Hathaway, *et al.*[10].

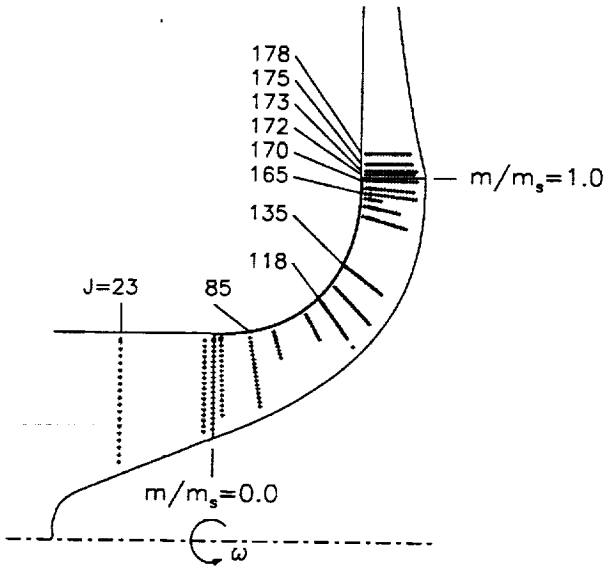

Figure 1 Meridional View of LSCC rotor showing laser anemometer measurement locations.

MEASUREMENT UNCERTAINTY

The uncertainty of the individual velocity component measurements was estimated from the least squares calculation to be on the average approximately ±1.5 m/sec throughout most of the impeller passage. Through much of the impeller passage, the throughflow velocity magnitude is on the order of 75 m/sec. Thus, the uncertainty of the measured velocity components is less than 2% of the throughflow component.

In addition to the propagation of uncertainties of the measured velocity components into the calculated velocity components, the measured velocity components are subject to the uncertainties arising from window curvature effects which distort the laser anemometer probe volume. The spanwise velocity component and flow pitch angle are most susceptible to uncertainty propagation and are therefore most sensitive to window curvature effects. As determined from Figure 2, the uncertainty in pitch angle, which directly indicates the ability to resolve the spanwise velocity component, is estimated to be less than ±2 degrees for measurement locations in the outer 70% of blade span for all measurement stations up to and including station 135. Because window curvature and blade span both decrease in the rear of the impeller, the uncertainty in the pitch angle for measurement stations 165-178 should be less than ±2 degrees over the entire blade span.

COMPUTATIONAL ANALYSIS

The computational results for the LSCC flow field were obtained using the Reynolds-averaged Navier-Stokes code developed by Dawes[4]. The solution grid has 137 streamwise points (75 points are within the blade) with clustering around the leading edge, 71 points spanwise with 4 volumes in the tip clearance, and 41 points pitchwise. The pitchwise spacing at mid-pitch is about 5 percent of pitch and the nearest points away from the blade surfaces are at about 1 percent of pitch (however, the cell centers are 0.5 percent pitch from the surfaces). The spanwise spacing varies from a maximum of about 5 percent of span at mid-span to 0.15 percent of span for the grid nodes nearest the hub and shroud (the cell centers are about 0.07 percent away from the endwalls). The maximum streamwise spacing is about 2.5 percent of meridional chord at mid-chord.

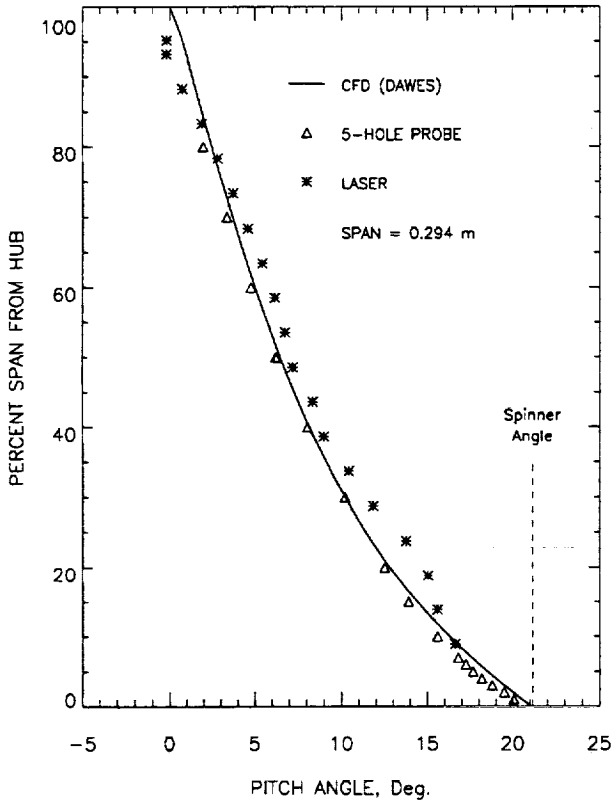

Figure 2 Measured and predicted pitch angle distribution at rotor inlet station J=23 (m/m_s=-0.397).

RESULTS AND DISCUSSION

Throughflow Development The streamwise development of the throughflow velocity will be illustrated through the use of "wire-frame" plots of the quasi-meridional velocity normalized by the rotor tip speed, V_{qm}/U_t. As described by Hathaway, *et. al.*[10], the quasi-meridional velocity V_{qm} approximates the throughflow velocity component at any cross-channel station in the impeller. In order to facilitate comparison of the CFD solution to the laser data, the CFD solution was interpolated in the streamwise and spanwise directions to correspond with the experimental measurement locations. The results in each plot are shown at every 5% of span, with the results nearest the shroud located at 95% of blade span from the hub, where 100% span denotes the blade tip.

The results obtained at station 118 (m/m_s = 0.47) are shown in Figure 3a. At this station, a region of low streamwise momentum appears near the shroud at about mid-pitch. This region has been referred to as the "wake" region by previous investigators (Eckardt[5]; Krain[12]). The wake is evident in the experimental data at both 90 and 95% span, but is only evident in the CFD solution at 95% span. Inspection of data which is not presented here indicates that the wake first begins to develop at mid-pitch at m/m_s = 0.40.

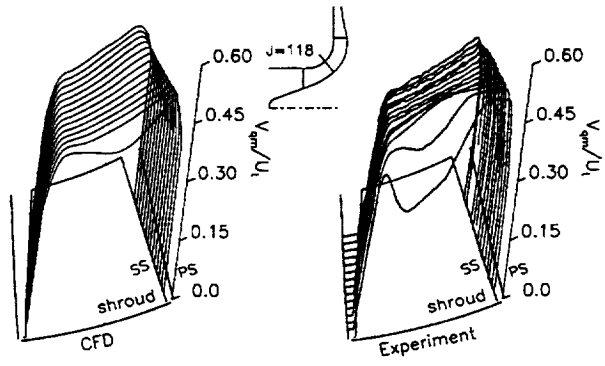

Figure 3a Distribution of normalized quasi-meridional velocity at station 118 (m/m_s=0.475) at intervals of 5% span starting at 95% span.

The results obtained at station 135, (m/m_s = 0.64) are shown in Figure 3b. The broken lines indicate additional results obtained at 1% span intervals from 96% to 100% span. The momentum deficit near the shroud in both the measurements and the CFD results continues to grow in magnitude. The wake centerline also moves toward the pressure side of the passage. The measured wake occupies the outer 25% of the span. Note that the CFD solution under-predicts both the maximum velocity deficit in the wake and the spanwise extent of the wake. Also note from Figures 3a,b that both the measured and predicted throughflow momentum in the portion of the passage which is outside the wake is nearly constant for stations 118 and 135.

At station 165, (m/m_s = 0.94) shown in Figure 3c, the measured throughflow velocity deficit in the wake is less severe than it was at station 135. However, the minimum wake velocity at 95% span is nearly unchanged between stations 135 and 165. A detailed inspection of the blade-to-blade distributions of the throughflow velocity, plotted at individual spanwise locations, indicates that the streamwise velocity throughout the lower half of the passage and near the suction surface in the upper half of the passage has dropped significantly relative to its level at station 135. This behavior makes the wake ap-

pear less severe at station 165 than at station 135. The CFD solution indicates the wake has grown to occupy a larger spanwise extent than at station 135 and that the predicted minimum wake velocity is now comparable to the measured wake minimum velocity. Station 165 is in the region of the impeller blade passage where the pressure surface is not "covered" by the suction surface. This region begins at m/m_s = 0.85. The observed increase in pressure surface velocity and decrease in suction surface velocity is expected as a result of unloading of the blade. There is also a shift of the wake centerline toward mid-pitch.

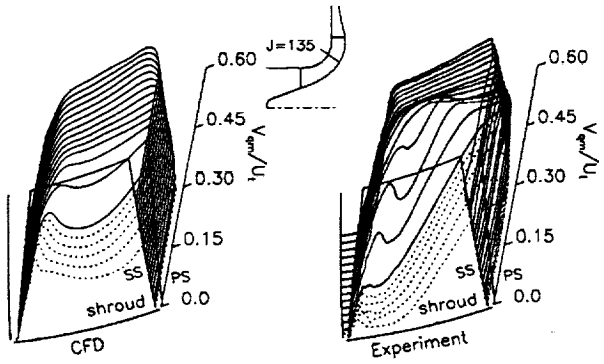

Figure 3b Distribution of normalized quasi-meridional velocity at station 135 (m/m_s=0.644). Solid lines at intervals of 5% span starting at 95% span. Broken lines at intervals of 1% span starting at 100% span.

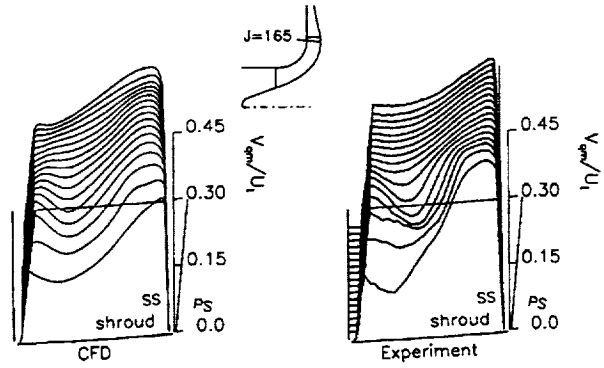

Figure 3c Distribution of normalized quasi-meridional velocity at station 165 (m/m_s=0.941) at intervals of 5% span starting at 95% span.

The results obtained at station 170 which is at a radius ratio of 0.99 are shown in Figure 3d. The CFD results agree qualitatively with the measurements. As we move from station 165 to station 170 we also note a continued unloading of the blade as well as a continued shift of the wake centerline toward mid-pitch. The shift in wake centerline location near the exit of the impeller results from a continuing increase in the throughflow velocity near the pressure surface with increasing downstream distance.

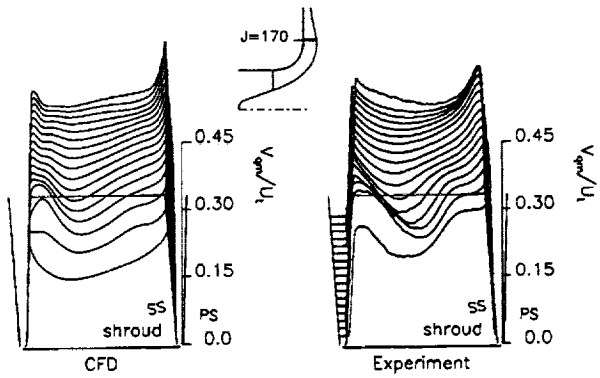

Figure 3d Distribution of normalized quasi-meridional velocity at station 170 (m/m_s=0.990) at intervals of 5% span starting at 95% span.

In summary, the results shown in Figure 3 indicate that the classic throughflow momentum deficit, or wake, which has been observed in centrifugal compressors by many other investigators occurs in the outer 25–35% of the span at the blade exit for this compressor. The wake is initially detected near mid-pitch, moves to the pressure surface/shroud corner of the passage, and then moves toward mid-pitch due to a continued increase in momentum in the pressure surface/shroud corner of the blade passage near the exit of the impeller.

The CFD solution predicts the location and strength of the wake near the impeller exit quite well, but under-predicts the maximum velocity deficit in the wake and the spanwise extent of the wake at stations 118 and 135. These features of the CFD solution are quite sensitive to the tip clearance model used in the code. The code models the vena-contracta formed by the clearance jet crossing the sharp blade edge by using a tip clearance value which is less than the physical tip clearance. The value used in the present solution is 60% of the physical tip clearance. The effect of increasing the tip clearance used in the code from 60% to 100% of the actual clearance has been studied using a slightly coarser grid (75 streamwise points in the blade, 41 points spanwise, 41 points pitchwise). The results indicate that increasing the tip clearance in the CFD solution does indeed result in an increase in the spanwise extent of the wake and moves the wake minimum velocity closer to the pressure surface at a given station. Inspection of the impeller blade tips at the conclusion of testing indicated that the blade tip corners were not sharp. A contraction coefficient of 0.6 is therefore too small.

Secondary Velocity Development "Secondary velocity" as used in this paper is defined as that component of the total relative velocity vector which is not aligned with streamwise CFD grid lines. A detailed definition of the spanwise and pitchwise secondary velocity components is provided by Hathaway, *et. al.*[10]. Measured and predicted secondary velocity vectors are calculated in the same way.

As in the previous section, the CFD results were interpolated to the streamwise and spanwise location of the laser measurements. In order to provide more details of the tip clearance flow, CFD results are also shown at 98% of blade span and

at 101% of blade span, which lies inside the tip clearance gap. The pitchwise location of each vector in the CFD results is fixed by the pitchwise location of the CFD grid nodes. Although the laser measurements were made at 200 points across the pitch, only the data at every third point is presented for the sake of clarity. The predicted and measured vectors are drawn to the same scale with a reference vector of length $0.5*U_t$ shown in each plot. The streamwise momentum outside of the wake region for measurement stations up to and including station 135 is on the order of $0.5*U_t$. The strength of the secondary flow relative to the throughflow can therefore be approximated by comparing the secondary velocity vector magnitudes to the reference vector magnitude in each plot.

Also shown on the predicted secondary velocity vector plots are the locations of CFD tracer particles which were released along the blade leading edge from hub to tip on either side of the leading edge stagnation line. The CFD tracer locations illustrate how low momentum fluid along the blade surface migrates toward the blade tip and becomes entrained in the tip clearance flow.

At station 118, shown in Figure 4a, both the CFD and experimental results indicate that the low momentum fluid near the blade suction surface is migrating outward toward the blade tip. The CFD solution also indicates a migration of fluid toward the tip along the pressure surface. However, the experimental results indicate that the fluid moving outward along the blade pressure surface is met and turned by fluid from the vortical flow near the shroud which is moving inward toward the hub near the pressure surface/shroud corner. The vortical flow near the shroud resides in approximately the same location as the low-momentum throughflow wake region indicated in Figure 3a. The CFD and experimental results do not provide a clear indication of the origin of the inward flow which is measured in the pressure surface/shroud corner. However, the CFD tracer locations indicate that tracer particles released on the suction and pressure surfaces at the blade leading edge, denoted by $*$'s and $\diamond$'s respectively, have become entrained within the tip clearance flow and are migrating toward the pressure surface. The inward flow in the blade pressure surface/shroud corner may therefore be a result of the tip clearance flow impinging on the blade pressure surface.

The secondary flow results obtained at station 135 are shown in Figure 4b. Both the CFD and experimental results indicate a continuing migration of fluid outward toward the tip near the blade surfaces. However, the CFD results indicate that the fluid migrating outward along the blade pressure surface is now being met and turned inward by fluid moving downward near the blade pressure surface/shroud corner, just as was shown in the experimental results at station 118. In addition, the CFD tracers show further migration toward the blade pressure surface and the tracers appear to be rolling up into a vortical flow. The experimental results now show a stronger vortical flow near the shroud than indicated at station 118.

The insets in Figure 4b show additional details of the measured and predicted flows in the tip region which, for the sake of clarity, are not provided in the full-size passage view. The vector scale is different for each inset and is chosen so as to minimize overlap among vectors. Details of the predicted results in the blade pressure surface/shroud corner are shown in the left inset of Figure 4b, which is a magnified view of the full-size passage results. The results show that the inward flow in the pressure surface/shroud corner of the passage is caused by the roll-up of endwall fluid near the tip of the blade. The middle inset of Figure 4b provides further details of the measured flow field from 95–100% span at the full pitchwise resolution of the laser anemometer measurements. The results verify the roll-up of fluid predicted by the CFD solution in the pressure surface/shroud corner and show the movement of fluid near the suction surface into the tip clearance gap. Finally, the right inset provides details measured within the blade suction surface boundary layer at 85, 90, and 95% span at the full pitchwise resolution of the laser anemometer mea-

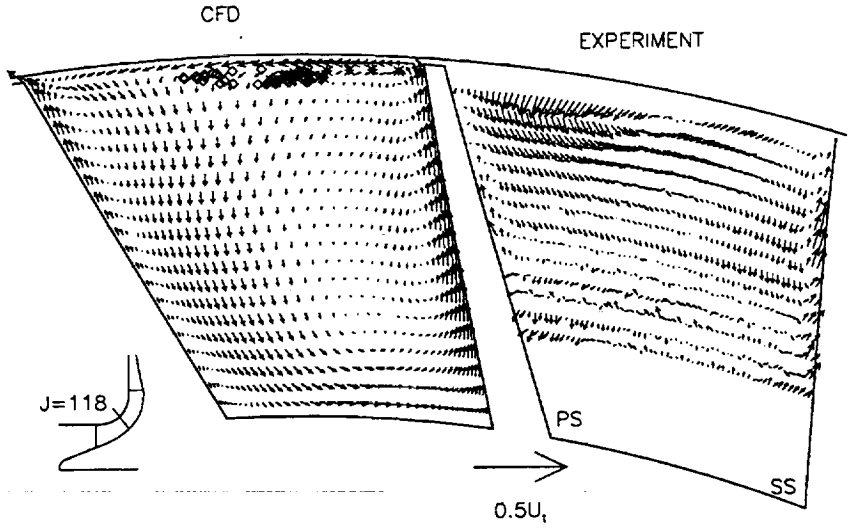

Figure 4a Secondary flow velocity vector plots at station 118 (m/m_s=0.475). Both CFD and experimental results shown at intervals of 5% span starting at 95% span with additional CFD results at 98% and 101% span. $\diamond$ and $*$ denote CFD tracers released along the blade leading edge on the pressure and suction surfaces, respectively.

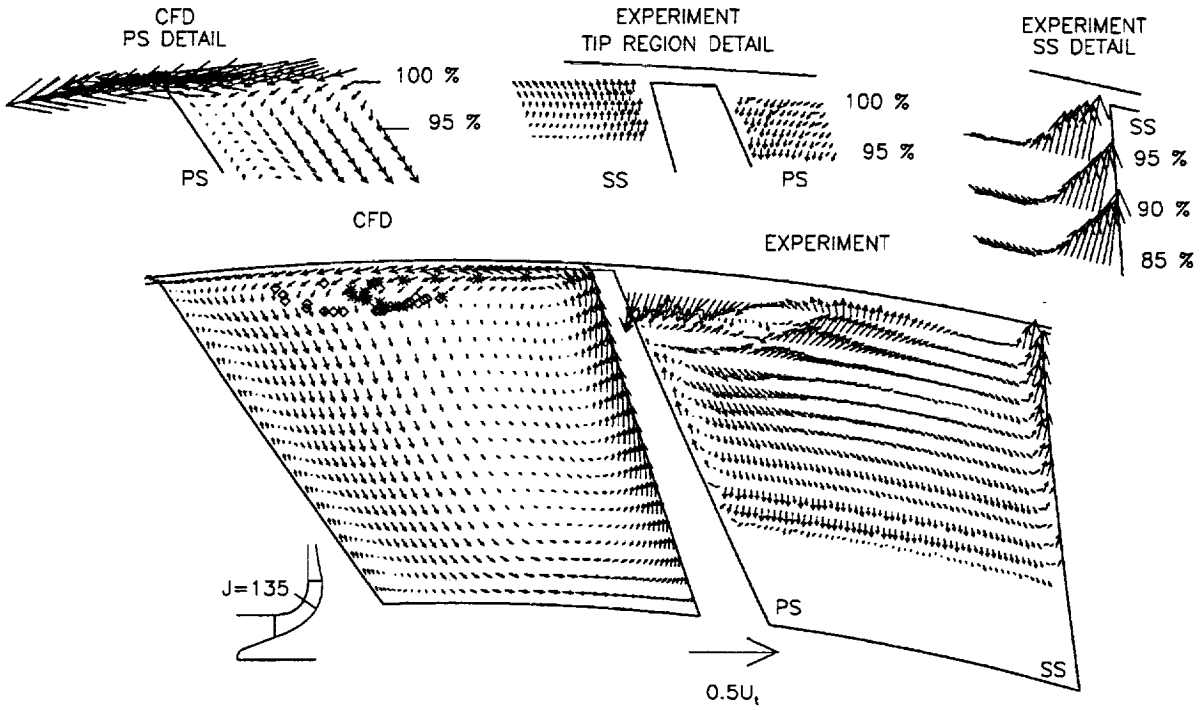

Figure 4b Secondary flow velocity vector plots at station 135 (m/m_s=0.644). Both CFD and experimental results shown at intervals of 5% span starting at 95% span with additional CFD results at 98% and 101% span. ◇ and ∗ denote CFD tracers released along the blade leading edge on the pressure and suction surfaces, respectively. Insets show additional qualitative details of the tip region flow using the actual CFD grid and full laser measurement resolution.

surements. The data clearly shows the migration of the suction surface boundary layer fluid toward the shroud.

A comparison of Figure 3b and Figure 4b indicates that there is once again a strong correlation between the location of the throughflow velocity deficit and the location of strong secondary flow. As shown in Figure 3b, the magnitude of the measured normalized throughflow velocity in the pressure surface/shroud corner of the passage is $V_{qm}/U_t = 0.10 — 0.15$. In this region the magnitude of the secondary flow is on a par with the throughflow velocity.

At station 165, shown in Figure 4c, the CFD solution indicates a continued migration of flow outward along the blade surfaces and a well-behaved roll-up of flow in the pressure surface/shroud corner of the passage. The experimental results do not indicate outflow along the suction surface of the blade as predicted by the CFD result. We also note that a weak but discernible outward flow appears in the measurements towards the pressure-side half of the passage below about 70% span. However, the most dominant measured flow features are the strong spanwise flows in the pressure surface/shroud corner with an apparent strong reversal in spanwise flow direction (to be addressed subsequently) at about 87% span. The measurements in this region were repeated on three separate occasions and each measurement session yielded identical results.

At station 170, shown in Figure 4d, we see a dramatic change in the measured secondary flow relative to that just shown at station 165. The outward flow near the blade pressure surface, which was located below about 70% span and was quite weak at station 165, now dominates the secondary flow field in the pressure surface/shroud corner.

In order to investigate the cause of the secondary flow results shown in Figure 4c, we inspected the statistics of the individual laser anemometer measurements acquired at each of the 200 measurement points across the blade pitch. At each point a probability density distribution (p.d.d.) was constructed for all of the measurements which occurred at that point. Throughout most of the flowfield, these p.d.d.'s are Gaussian in character, which is to be expected for a turbulent flow. However, for points in the pressure surface/shroud corner at station 165, the p.d.d.'s are skewed, with long "tails" which result from the occurrence of velocities that are well below the mean velocity. The averaging method used to process all of the laser anemometer data essentially calculates the mean of each p.d.d. For Gaussian p.d.d.'s the mode, defined as the velocity which occurs most often, is close to or identical to the mean. However, for the p.d.d.'s which are skewed toward lower velocities, the mean occurs at a lower velocity than the mode.

The secondary velocity vectors shown in the inset in Figure 4c are calculated using the mode of each p.d.d. rather than the mean. The mode results yield a secondary velocity field which has no vortical structure and is more similar to that measured at station 170. Since the mode is by definition the velocity which occurs most often, the mode results are felt to be more representative of the secondary velocity field in the pressure surface/shroud corner at station 165.

The skewed p.d.d.'s in the pressure surface/shroud corner suggest that the flow is quasi-steady in this region. This might

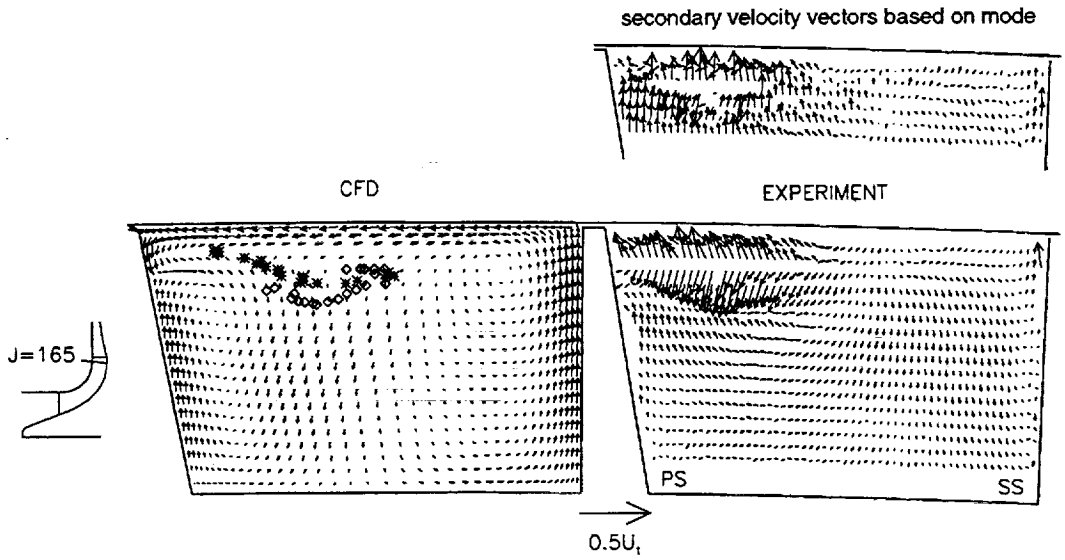

Figure 4c Both CFD and experimental results shown at intervals of 5% span starting at 95% span with additional CFD results at 98% and 101% span. ◇ and * denote CFD tracers released along the blade leading edge on the pressure and suction surfaces, respectively. Secondary flow velocity vector plots at station 165 (m/m_s=0.941).

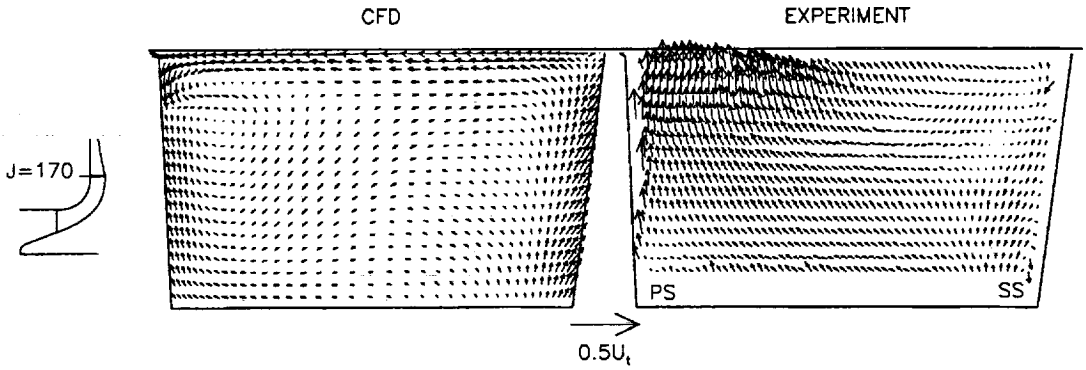

Figure 4d Secondary flow velocity vector plots at station 170 (m/m_s=0.990). Both CFD and experimental results shown at intervals of 5% span starting at 95% span with additional CFD results at 98% and 101% span. ◇ and * denote CFD tracers released along the blade leading edge on the pressure and suction surfaces, respectively.

be caused by a "meandering" of the throughflow wake at station 165. The secondary velocity vectors at stations 135 and 170 were also calculated based on the mode of the p.d.d.'s. The results, which are not included here, indicate that there is no appreciable difference between the vectors calculated using the mode and those calculated using the mean. These results indicate that the flow is steady at stations 135 and 170.

The results at station 135 indicate the development of a vortex which does not appear at stations 165 and 170. The ability to "see" a vortex is highly dependent on the viewing direction used when creating the secondary velocity vectors. The fact that a vortex appears at station 135 indicates that the vortex core is well aligned with the streamwise grid lines at that station. The results shown in Figure 3 indicate that the throughflow velocity wake drifts from a location near the pressure surface toward mid-pitch as we move from station 135 to stations 165 and 170. If the vortex is associated with the wake, then the vortex core might also drift toward mid-pitch in the rear of the rotor. The vortex might therefore still be present at stations 165 and 170 but is no longer evident in the secondary velocity vector plots because the core is no longer aligned with the streamwise grid lines. The secondary velocities at stations 135, 165, and 170 were viewed from different directions and the general features of the secondary velocities were found to be relatively insensitive to viewing angle.

A perspective view of the CFD particle trace results is presented in Figure 5, which shows the predicted trajectories of the particles which are released from hub to tip along the blade leading edge on either side of the leading edge stagnation line. The view in Figure 5 is as viewed looking upstream into the impeller blade passage from a viewpoint near the impeller exit. The black traces in passage 1 are the trajectories of particles released on the suction surface in blade passage 1. These particles migrate up the blade surface toward the tip, are entrained in the tip clearance jet and transported across the blade passage near the shroud, and then begin to roll up in the pressure surface/shroud corner of passage 1. This roll-up

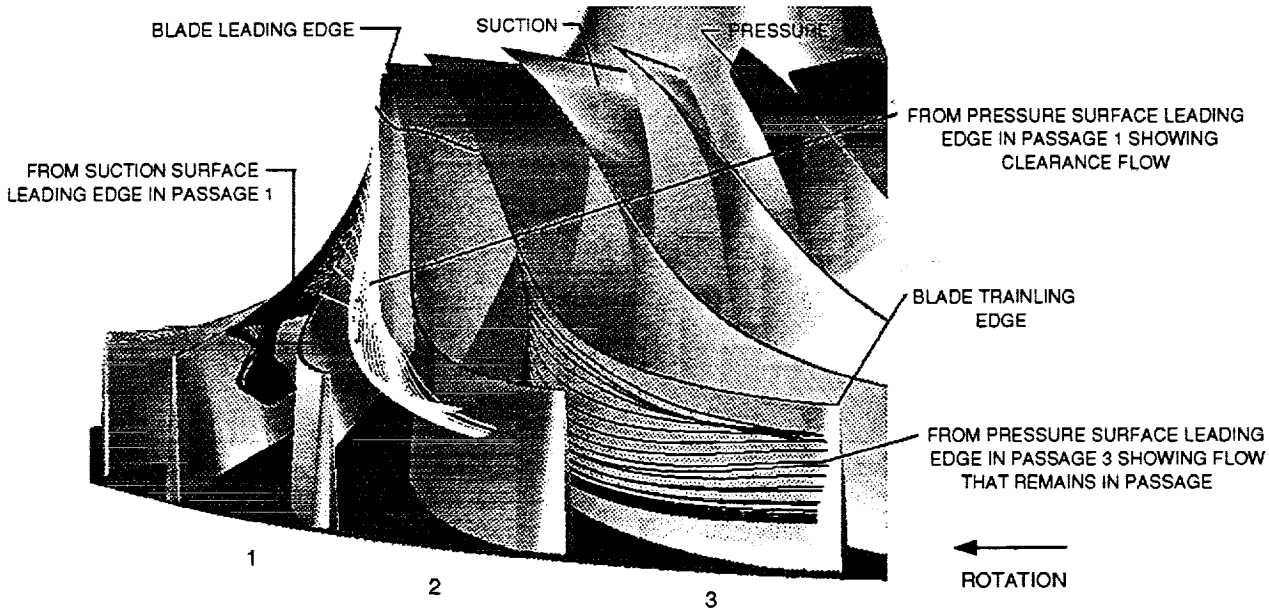

Figure 5 Perspective view of the paths of CFD tracers released on the blade surfaces near the impeller leading edge.

can be clearly seen in Figure 5 and also in both the CFD solution and the laser measurements at station 135 (Figure 4b). The white traces in Figure 5 are the trajectories of particles released in blade passage 1 on the pressure surface outboard of 63% span. These particles migrate toward the tip, cross over the blade, move across the passage near the shroud, and roll up in the pressure surface/shroud corner in passage 2. The migration of pressure surface fluid across the tip can also be seen in the CFD solution at station 118 (Figure 4a). The black traces in passage 3 in Figure 5 are the trajectories of particles released in blade passage 3 on the pressure surface inboard of 63% span. These particles begin to migrate toward the tip but are met and turned inward by the fluid which rolls up in the pressure surface/shroud corner. This behavior can also be seen in the CFD results shown in Figures 4b,c at stations 135 and 165. Comparison of the particle trajectories in Figure 5 with the throughflow velocity results of Figure 3 clearly demonstrates that the throughflow velocity wake is formed by the migration of low momentum fluid near the blade surfaces toward the shroud where it is entrained by the tip clearance flow and transported toward the pressure surface.

We have studied the trajectories of additional CFD tracers released all along the blade chord on the blade surfaces near the tip. These trajectories, which are not shown here, indicate that all of the fluid outboard of the tracers shown in Figure 4 originated on the blade surfaces. The tracer locations shown in Figure 4 therefore define the lower bound of the tip clearance flow.

The secondary flow field results presented thus far have qualitatively illustrated the features of the secondary flow field and the comparison between CFD and experimental results. A more quantitative comparison between CFD and experimental results will now be provided by presenting blade-to-blade distributions of velocity and pitch angle at selected measurement locations at stations 118 and 165.

The measured and predicted distributions of the normalized quasi-meridional velocity, normalized spanwise secondary velocity, and pitch angle at 65% span at station 118 are shown in Figure 6. The comparison between predicted and measured values of V_{qm}/U_t, which approximates the throughflow velocity, are excellent. The extent of the suction and pressure surface boundary layers are clearly shown. The laser anemometer measurements of the normalized spanwise secondary velocity, V_s/U_t, (see Figure 6b) indicate appreciable outflow near both the pressure and suction surfaces and a weak inflow across the remainder of the passage. Note that the outflow regions shown in Figure 6b closely correspond to the blade boundary layers shown in Figure 6a.

The ability of the laser measurements to accurately resolve the spanwise velocity component is illustrated in Figure 6c where we see that the pitch angles, α, measured on the blade surfaces with an ammonia/ozalid flow visualization technique are in close agreement with the near-surface pitch angles measured with the laser anemometer.

Measured and predicted pitch angle distributions as well as the ammonia/ozalid surface flow angle results at 20, 80 and 95% span for station 165 are shown in Figure 7. At 80 and 95% span the pitch angle distributions derived from both the mean and mode of the laser measurements are shown. As discussed previously, the mode results are considered to be more representative of the flow in this region than are the mean results. The grid normal at station 165 has a pitch angle of 85 degrees. Therefore, a flow pitch angle which is greater than 85 degrees indicates a spanwise flow toward the shroud while a flow pitch angle which is less than 85 degrees indicates a spanwise flow toward the hub.

There is no appreciable spanwise flow across the entire passage at the 20% span location. The laser measurements do not indicate a large change in flow angle near the pressure surface between 80 and 95% span. However, the CFD and ammonia/ozalid results indicate a change in pitch angle on the pressure surface on the order of 50 degrees between these two

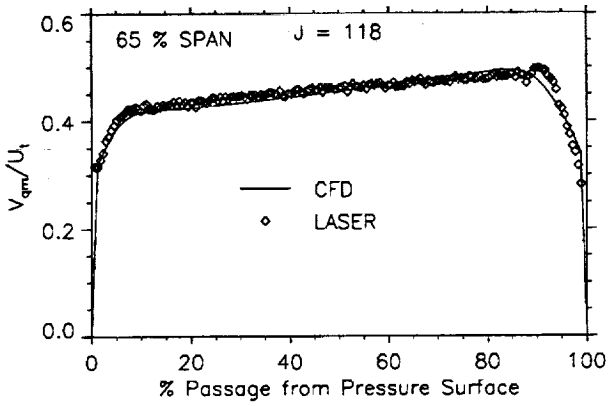

Figure 6a Blade-to-blade distribution of normalized quasi-meridional velocity at 65% blade span for station 118 (m/m_s=0.475).

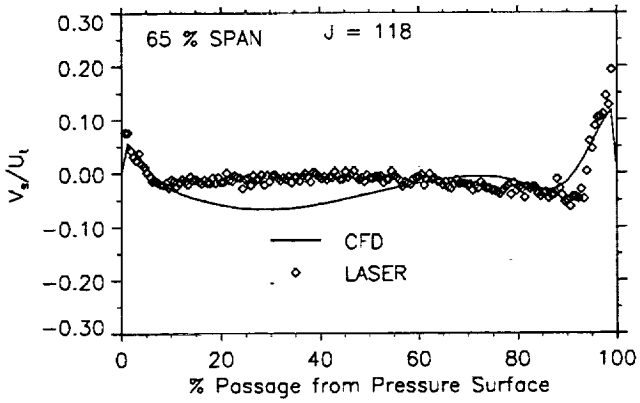

Figure 6b Blade-to-blade distribution of normalized spanwise secondary velocity at 65% blade span for station 118 (m/m_s=0.475).

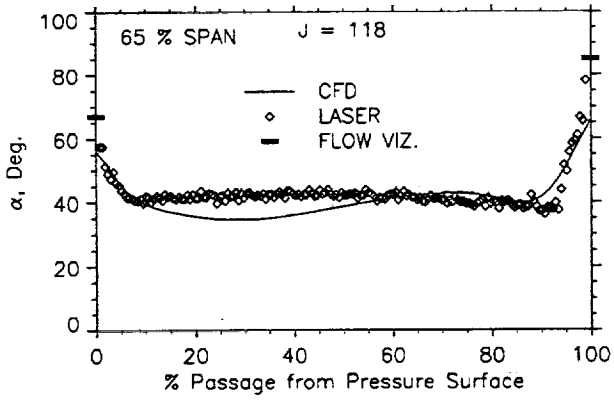

Figure 6c Blade-to-blade distribution of flow pitch angle at 65% blade span for station 118 (m/m_s=0.475).

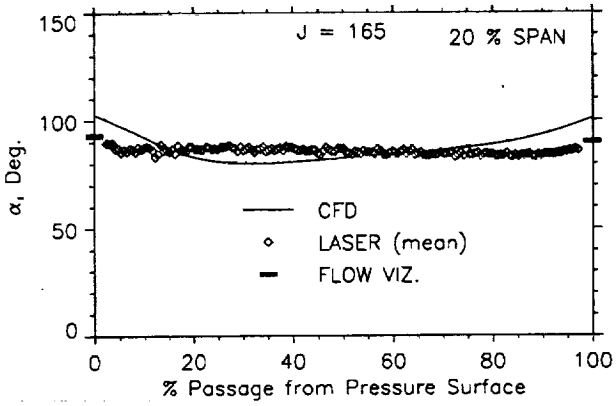

Figure 7a Blade-to-blade pitch angle distributions at 20% blade span for station 165 (m/m_s=0.941).

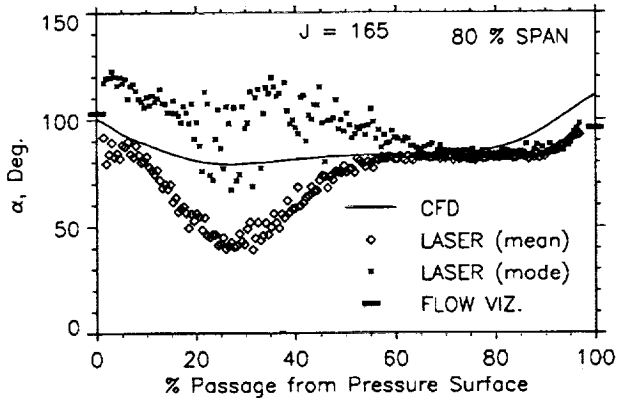

Figure 7b Blade-to-blade pitch angle distributions at 80% blade span for station 165 (m/m_s=0.941).

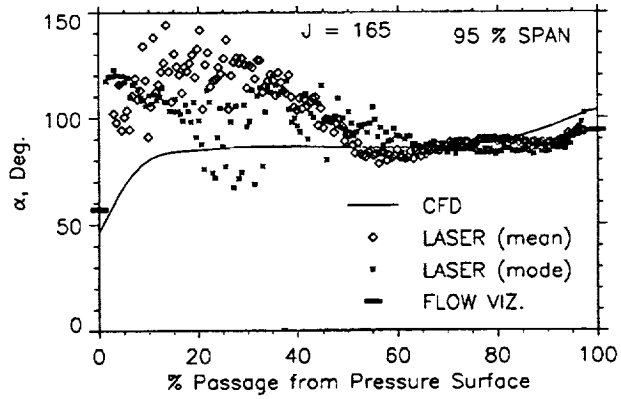

Figure 7c Blade-to-blade pitch angle distributions at 95% blade span for station 165 (m/m_s=0.941).

spanwise locations. Note that all three techniques also indicate a relatively weak spanwise flow along the suction surface at all immersions.

SUMMARY AND CONCLUSIONS

The results presented herein represent an extensive computational and experimental effort to document the velocity field within the NASA Low Speed Centrifugal Compressor (LSCC). The large impeller passage size provides considerable optical access to the flow field and enables measurements of the three—dimensional velocity field throughout the impeller blade passage. In several cases the measurements provide details within the blade boundary layers.

The laser anemometer measurements and the CFD solution complement one another in illustrating the flow physics within the impeller. Laser anemometer measurements confirm that the low momentum fluid near the blade surfaces migrates outward toward the tip of the blade as predicted by the CFD solution. Particle traces done on the CFD solution indicate that the fluid which moves up the blade pressure and suction surfaces is entrained into the tip clearance jet. The particle traces also show that this fluid is then transported toward the pressure side/shroud corner of the passage, where it contributes to the formation of the characteristic throughflow momentum wake which is found in unshrouded centrifugal compressor impellers.

The experimental results presented provide a representative view of the flow physics within unshrouded centrifugal compressor impellers and should be useful in assessing the ability of viscous flow codes to accurately predict the flow physics within centrifugal compressors.

REFERENCES

1 Ahmed, N. A. and Elder, R. L., "Flow Investigation in a Small High Speed Impeller Passage Using Laser Anemometry," ASME Paper No. 90-GT-233, 1990.

2 Baldwin, B. and Lomax, H., "Thin Layer Approximation and Algebraic Model for Separated Turbulent Flows," AIAA Paper 78-257, 1970.

3 Bansod, P., and Rhie, C. M., "Computation of Flow Through a Centrifugal Impeller with Tip Leakage," AIAA Paper No. 90–2021, 1990.

4 Dawes, W. N., "Development of a 3-D Navier Stokes Solver of Application to all Types of Turbomachinery," ASME Paper 88-GT-70, 1988.

5 Eckardt, D., "Detailed Flow Investigations Within a High-Speed Centrifugal Compressor Impeller," ASME Journal of Fluids Engineering, Vol. 98, 1976, pp. 390-402.

6 Fagan, J. R., and Fleeter, S., "Impeller Flow Field Measurement and Analysis," ASME Journal of Turbomachinery, Vol. 113, No. 4, 1991, pp. 670–179.

7 Farge, T. Z., Johnson, M. W., and Maksoud, T. M. A., "Tip Leakage in a Centrifugal Impeller," ASME Journal of Turbomachinery, Vol. 111, 1989, pp. 244-249.

8 Hah, C., and Krain, H., "Secondary Flows and Vortex Motion in a High- Efficiency Backswept Impeller at Design and Off-Design Conditions," ASME Journal of Turbomachinery, Vol. 112, 1990, pp. 7-13.

9 Hathaway, M. D., Wood, J.R., and Wasserbauer, C.W., "NASA Low Speed Centrifugal Compressor for 3-D Viscous Code Assessment and Fundamental Flow Physics Research," ASME Paper No. 91–GT–140, 1991.

10 Hathaway, M. D., Chriss, R. M., Wood, J.R., and Strazisar, A. J., "Experimental and Computational Investigation of the NASA Low-Speed Centrifugal Compressor Flow Field," ASME Journal of Turbomachinery, Vol. 115, No. 3, July 1993, pp. 527–542.

11 Joslyn, H. D., and Dring, R. P., "Surface Indicator and Smoke Flow Visualization Techniques in Rotating Machinery," Heat Transfer and Fluid Flow in Rotating Machinery, Hemisphere Publishing Corp., 1986, pp. 156–169.

12 Krain, H., "Swirling Impeller Flow," ASME Journal of Turbomachinery, Vol. 110, pp. 122-128.

13 Krain, H. and Hoffman, W., 1989, "Verification of an Impeller Design by Laser Measurements and 3D-Viscous Flow Calculations," ASME Paper No. 89–GT-159, 1988.

14 Krain, H. and Hoffman, W., "Centrifugal Impeller Geometry and its Influence on Secondary Flows," in AGARD Secondary Flows in Turbomachines, 1990."

15 Moore, J. and Moore, J. G., "A prediction of 3-D Viscous Flow and Performance of the NASA Low-Speed Centrifugal Compressor," ASME Paper No. 90-GT-234, 1990.

16 Rohne, K. H., and Banzhaf, M., "Investigation of the Flow at the Exit of an Unshrouded Centrifugal Impeller and Comparison With the "Classical" Jet-Wake Theory," ASME Journal of Turbomachinery, Vol 113, No. 4, 1990, pp 654–659.

17 Senoo, Y., Yamaguchi, M., and Nishi, M., "A Photographic Study of Three-Dimensional Flow in a Radial Compressor," ASME Paper No. 68-GT-2, 1968.

18 Sipos, G., Secondary Flow Loss Distribution in a Radial Compressor with Untwisted Backswept Vanes," ASME Journal of Turbomachinery, Vol 113, No. 4, 1991, pp 686–695.

19 Wood., J. R., Adam, P. W., and Buggele, A. E., "NASA Low-Speed Centrifugal Compressor for Fundamental Research," NASA TM 83398, 1983.

REPORT DOCUMENTATION PAGE

Form Approved
OMB No. 0704-0188

1. AGENCY USE ONLY (*Leave blank*)	2. REPORT DATE	3. REPORT TYPE AND DATES COVERED
	December 1993	Technical Memorandum

4. TITLE AND SUBTITLE
Experimental and Computational Results From a Large Low-Speed Centrifugal Impeller

5. FUNDING NUMBERS
WU–505–62–52
1L161102AH45

6. AUTHOR(S)
M.D. Hathaway, R.M. Chriss, J.R. Wood, and A.J. Strazisar

7. PERFORMING ORGANIZATION NAME(S) AND ADDRESS(ES)
NASA Lewis Research Center
Cleveland, Ohio 44135–3191
and
Vehicle Propulsion Directorate
U.S. Army Research Laboratory
Cleveland, Ohio 44135–3191

8. PERFORMING ORGANIZATION REPORT NUMBER
E–8258
ARL–TR–331

9. SPONSORING/MONITORING AGENCY NAME(S) AND ADDRESS(ES)
National Aeronautics and Space Administration
Washington, D.C. 20546–0001
and
U.S. Army Research Laboratory
Adelphi, Maryland 20783–1145

10. SPONSORING/MONITORING AGENCY REPORT NUMBER
NASA TM–106421

11. SUPPLEMENTARY NOTES
Prepared for the 82nd Meeting of the AGARD Propulsion and Energetics Panel, Technology Requirements for Small Gas Turbine Engines, sponsored by the Advisory Group for Aerospace Research and Development, Montreal, Canada, October 4–6, 1993. M.D. Hathaway, Vehicle Propulsion Directorate, U.S. Army Research Laboratory, Lewis Research Center, Cleveland, Ohio 44135; and R.M. Chriss, J.R. Wood, and A.J. Strazisar, NASA Lewis Research Center. Responsible person, M.D. Hathaway, (216)433–6250.

12a. DISTRIBUTION/AVAILABILITY STATEMENT
Unclassified - Unlimited
Subject Category 02

12b. DISTRIBUTION CODE

13. ABSTRACT ***(Maximum 200 words)***

An experimental and computational investigation of the NASA Low-Speed Centrifugal Compressor (LSCC) flow field has been conducted using laser anemometry and Dawes' 3D viscous code. The experimental configuration consists of a backswept impeller followed by a vaneless diffuser. Measurements of the three-dimensional velocity field were acquired at several measurement planes through the compressor. The measurements describe both the throughflow and secondary velocity field along each measurement plane and in several cases provide details of the flow within the blade boundary layers. The experimental and computational results provide a clear understanding of the development of the throughflow momentum wake which is characteristic of centrifugal compressors.

14. SUBJECT TERMS
Centrifugal compressors; Radial turbomachinery; Laser velocimetry; Computational fluid dynamics

15. NUMBER OF PAGES
12

16. PRICE CODE
A03

17. SECURITY CLASSIFICATION OF REPORT	18. SECURITY CLASSIFICATION OF THIS PAGE	19. SECURITY CLASSIFICATION OF ABSTRACT	20. LIMITATION OF ABSTRACT
Unclassified	Unclassified	Unclassified	